mater.scichina.com link.springer.com

Published online 10 January 2023 | https://doi.org/10.1007/s40843-022-2287-7
*Sci China Mater* 2023, 66(5): 2061–2070

# Strong high-entropy diboride ceramics with oxide impurities at 1800°C

Jie Liu[1,2], Qing-Qing Yang[1,3], Ji Zou[1,2*], Wei-Min Wang[1,2], Xin-Gang Wang[3*] and Zheng-Yi Fu[1,2*]

**ABSTRACT** **In this study, a type of high-entropy boride (HEB) ceramics ($(Ti_{0.2}Zr_{0.2}Nb_{0.2}Hf_{0.2}Ta_{0.2})B_2$) with ~2 vol% oxides and ~1 vol% porosity was successfully consolidated by spark plasma sintering at 2000°C under a uniaxial load of 50 MPa for 10 min, using self-synthesized high entropy diboride powders from a boro/carbothermal reduction approach. The residual oxides were determined to be m-$(Hf,Zr)O_2$, which were incorporated with minor amounts of boron and carbon. Elastic modulus, Vickers hardness and fracture toughness of HEBs at room temperature were 508.5 GPa, 17.7 ± 0.4 GPa and 4.2 ± 0.2 MPa $m^{1/2}$, respectively. The as-obtained ceramics possessed excellent flexural strength, particularly at high temperatures. The four-point flexural strengths of HEBs at room temperature, 1600, and 1800°C are 400.4 ± 47.0, 695.9 ± 55.9, and 751.6 ± 23.2 MPa, respectively. Postmortem analysis was conducted on HEB fractured at 1800°C, in the region near their tensile and fracture surfaces, and microstructure observations show that limited dislocation lines were present adjacent to the crack front and edge of the pore, without noticing any trace for dislocation motions. It is the first report on the high-temperature strength of high-entropy diboride ceramics and the strengthening mechanism at high temperatures was also discussed.**

**Keywords:** borides, high-entropy ceramics, high-temperature strength, mechanical properties, microstructure

## INTRODUCTION

In recent years, due to a rapid development of aerospace industry, the development of materials for key parts on aerospace vehicles that can be reused under super-high-speed flight conditions has become a top priority [1]. Challenges have arisen for creating a kind of materials possessing both excellent high-temperature oxidation resistance and high-temperature strength. As both requirements can be met by ultra-high-temperature ceramics (UHTCs), the research on UHTCs is therefore put on the agenda. Although UHTCs include refractory borides, carbides and nitrides of transition metals [2–7], transition borides attract more interest due to their better oxidation resistance and high thermal conductivity [8–13].

Entropy stabilization, a concept whereby at least three other elements in approximately equal ratios are added to a binary compound, has been used to produce stable, high-entropy borides (HEBs) [14–18]. For example, Feng *et al.* [14] produced $(Ti_{0.2}Zr_{0.2}Nb_{0.2}Hf_{0.2}Ta_{0.2})B_2$ powders by the boro/carbothermal reduction (BCTR) of desired oxides, $B_4C$ and carbon at 1650°C for 3 h. As-synthesized powders with low oxygen and carbon contents were densified at 2100°C for 10 min to achieve dense and pure HEB ceramics with fine grain sizes. Luo's group [15] firstly reported that $WB_2/MoB_2$-containing HEBs consolidated by reactive sintering are even harder than HEBs composed of harder binary boride components. Guo's group [16] prepared HEB with a relative density as high as 96.3%–98.5% combining BCTR and spark plasma sintering (SPS), resulting in relatively higher Vickers hardness. Nevertheless, the focus of these studies is mainly on the powder synthesis, process, and densification behavior of HEB, with less concern for their mechanical properties, particularly for flexural strength at high temperatures.

Flexural strength describes the ability of a material to resist failure in bending, which is considered as one of the most important parameters to evaluate the service of UHTCs in the demanding environment [19]. Unfortunately, the reports on the strength data of HEB are rare, and these values (322–581 MPa) [13,20] are generally lower than those for monolithic $ZrB_2$, $TiB_2$, etc. As regards high-entropy carbides (HECs), on the contrary, they have been reported to possess excellent high-temperature flexural strength [21], although Tamas *et al.* [22] found the existence of submicron-sized pores in the grains of HEC can sharply reduce their room-temperature (RT) strength. Recently, HECs exhibiting better creep resistance than monocarbides have also been confirmed [23]. A combination of the above studies indicates the strengthening of HECs is possible through the "core effects" of high-entropy materials, such as severe lattice distortion and sluggish diffusion. Considering the similarities between HECs and HEBs, HEBs with better performance at higher temperatures should be expected.

Oxide impurities are often found in the sintered HEBs and HECs [24,25]. For example, Luo's group [26] has prepared $(Hf_{0.2}Zr_{0.2}Ta_{0.2}Mo_{0.2}Ti_{0.2})B_2$, $(Hf_{0.2}Zr_{0.2}Ta_{0.2}Nb_{0.2}Ti_{0.2})B_2$ and $(Hf_{0.2}Zr_{0.2}W_{0.2}Mo_{0.2}Ti_{0.2})B_2$ ceramics through SPS. Diffraction results, scanning electron microscopy (SEM) images, and elemental mappings all reveal the presence of $(Zr,Hf)O_2$ in those sintered bodies. Guo's group [27,28] also reported the $(Zr,Hf)O_2$ impurity phase can be detected in the powders of $(Hf_{0.2}Zr_{0.2}Ta_{0.2}Cr_{0.2}Ti_{0.2})B_2$ and $(Hf_{0.2}Mo_{0.2}Zr_{0.2}Nb_{0.2}Ti_{0.2})B_2$ after borothermal reduction at 1600°C. Unfortunately, oxides are known to negatively affect the processing and properties of the boride. Previous investigations on $ZrB_2$ ceramics suggest the presence of oxide contaminations on the surfaces of boride powders could prevent their pressureless densification behavior [8,20,29,30].

[1] State Key Laboratory of Advanced Technology for Materials Synthesis and Processing, Wuhan University of Technology, Wuhan 430070, China
[2] Hubei Longzhong Laboratory, Xiangyang 441000, China
[3] Shanghai Institute of Ceramics, Chinese Academy of Sciences, Shanghai 201899, China
* Corresponding authors (emails: ji.zou@whut.edu.cn (Zou J); xgwang@mail.sic.ac.cn (Wang XG); zyfu@whut.edu.cn (Fu ZY))

  

The degradation on the flexure strength of $ZrB_2$ ceramics is also partially related to the oxide impurities [13]. Due to the softening of oxides at elevated temperatures, the grain boundary sliding of boride under the bending stress was accelerated. As a representative material in HEB, the processing of $(Ti_{0.2}Zr_{0.2}Nb_{0.2}Hf_{0.2}Ta_{0.2})B_2$ ceramics has been intensively investigated [31–33]; however, their high-temperature strengths have yet to be explored.

The purpose of this paper is to investigate the mechanical properties including high-temperature flexure strength of $(Ti_{0.2}Zr_{0.2}Nb_{0.2}Hf_{0.2}Ta_{0.2})B_2$. By carefully studying their microstructure, the strengthening mechanism of HEBs at high temperatures has been proposed.

## EXPERIMENTAL SECTION

Commercially available $TiO_2$ (99.9% purity, 30 nm, Aladdin, China), $ZrO_2$ (99.9% purity, 50 nm, CSG Holding, China), $HfO_2$ (99.9% purity, 300 nm, Founder Star, China), $Nb_2O_5$ (99.9% purity, Aladdin, China), $Ta_2O_5$ (99.9% purity, Aladdin, China), and $B_4C$ (96.8% purity, 0.6–1.2 μm, H. C. Starck, MA) powders were used in this study. The powder synthesis procedures *via* BCTR are similar to that described in our previous study [34]; the only difference is a graphite furnace was used to prepare the HEB powders, instead of an SPS facility, in order to enlarge the powder production capacity per run. A loose block containing $TiO_2/ZrO_2/Nb_2O_5/HfO_2/Ta_2O_5/B_4C$ with a molar ratio of 2/2/1/2/1/8.17 was heat treated at 1650°C for 1.5 h in vacuum (~10 Pa). As-obtained powders were finely ground in an agate mortar until they could pass through a 200-mesh sieve. Sintering was conducted in an SPS furnace (FCT HPD 25; FCT Systeme GmbH, Rauenstein, Germany) at 2000°C for 10 min in vacuum, using a heating rate of 100 K $min^{-1}$. A load of 50 MPa was applied to the samples at 1650°C, which was released upon cooling.

Thermodynamic calculations were conducted *via* Factsage package 8.1, using the SpMCBN database [35,36]. In order to better examine the microstructure, sintered ceramics were cut, ground, and polished. The surface of the polished specimen was investigated using SEM (Hitachi S-4800, Tokyo, Japan), and its phase assemblage was examined by X-ray diffraction (XRD, Empyrean, Panalytical, Netherlands). The detailed microstructure and local composition of as-sintered ceramics were investigated by a spherical aberration-corrected transmission electron microscopy (TEM, Titan G2 300, Thermo Fisher Scientific, USA) and energy electron loss spectrum (EELS, GIF 963, Gatan, USA). EELS data were acquired at 0.25 eV/channel and the energy range was 95–607 eV. Focused ion beam (FIB, Helios 450S FEI) was used for preparing TEM samples from fractured bars after testing at RT and 1800°C. The qualitative and distribution status of all the elements were analyzed by an electron probe micro-analyzer (EMPA, JXA-8230, Japan). Achimedes' principle was applied to measure the density of as-sintered ceramics using deionized water as the replacement media. A modulus-analyzed machine (GrindoSonic, Model MK7, Belgium) and a Vickers Hardness Tester (Durascan50, Struers, Austria) were used to determine the modulus and the Vickers hardness, respectively. The hardness values were tested under five different loads (0.2, 0.5, 1.0, 2.0, and 5.0 kg), and a fixed holding period of 15 s was chosen. Anstis equation was employed for calculating the indentation fracture toughness, based on the crack generated by the indents under 19.8 and 49.0 N. The flexure strength was measured in a four-point flexural mode (AG-X Plus, Shimadzu, Japan) at RT, 1600, and 1800°C, using crosshead speeds of 0.5, 2.5, and 5.0 mm $min^{-1}$, respectively. Dimensions of the bars were 25 mm × 2.5 mm × 2 mm (length by width by thickness). For simplicity, the bars tested at RT, 1600, and 1800°C were called HEB-RT, HEB-16, and HEB-18, respectively.

## RESULTS AND DISCUSSION

### Microstructure and phase assemblage

Typical microstructures of HEB observed from its polished surfaces are shown in Fig. 1a, b. Examination of SEM images revealed the sample was composed of relatively dense matrix (in a gray contrast), second phase in spherical shapes (in a brighter contrast) and residual pores (in a darker contrast). Based on the image analysis, the area ratio of the matrix, pores and spherical particles is approximately equal to 97:1:2, whilst the averaged size for the HEB grains, spherical particles and pores are 2.95 ± 0.3, 0.8 and 0.5 μm, respectively. Achimedes density of SPSed HEBs was measured to be 8.04 g $cm^{-3}$. Using a theoretical density value of 8.28 g $cm^{-3}$, it was calculated that HEBs contained ~2.91% porosity, which is slightly higher than the value (~1%) determined from the image analysis.

The XRD pattern of as-fabricated HEBs is presented in Fig. 1c, d. A series of peaks belonging to the $AlB_2$ structure with a space group of *P6/mmm* were indexed, which should be assigned to HEB. In Fig. 1c, some inconspicuous bumps between 30° and 40° were also observed from the XRD pattern, which shares similar peak positions as m-$HfO_2$ and t-$HfO_2$, albeit a slight peak shift to high angles was seen, indicating atoms with larger radius had been doped into the lattice of $HfO_2$. Combining the information given by XRD and SEM, the spherical particles detected in Fig. 1a should be $(Hf,M)O_2$-based solid solutions. This conclusion is in agreement with their contrast information displayed in Fig. 1a: oxides should be brighter than diborides due to their larger average atomic numbers.

### Elemental distribution in HEB

Distributions of different elements in HEBs were investigated *via* electron probe microanalysis-wavelength dispersive X-ray spectroscopy (EPMA-WDS) mapping as shown in Fig. 2. It is apparent that the spherical particles have a substantially higher concentration of oxygen and hafnium compared with those in the matrix. The standard Gibbs free energy of formation for various oxides decreases in an order of $TiO_2 > Nb_2O_5 > Ta_2O_5 > ZrO_2 > HfO_2$; hence, hafnia is the most stable oxides among them, reflecting its more refractory nature. Accordingly, the reduction of hafnia by $B_4C$ is the most difficult, resulting in their retention in HEBs. In the matrix, the composition is largely uniform apart from niobium. This may be due to the fact that niobium has a larger atomic radius (2.08 Å) than other metallic atoms and therefore is less prone to be incorporated into the high-entropy solid solution.

The Nb-rich phase separation from HEBs could also be supported *via* thermodynamic calculations as displayed in Fig. 3. With increasing temperature, the mixture containing five one-mole diborides ($TiB_2$, $ZrB_2$, $NbB_2$, $HfB_2$, and $TaB_2$) inclined to form two types of quinary diboride solid solutions, i.e., $MB_2$#1 and $MB_2$#2. Although both contained five diborides, $MB_2$#1 is rich in $ZrB_2$ and $HfB_2$, whilst the levels of $TiB_2$, $TaB_2$, and $NbB_2$

  

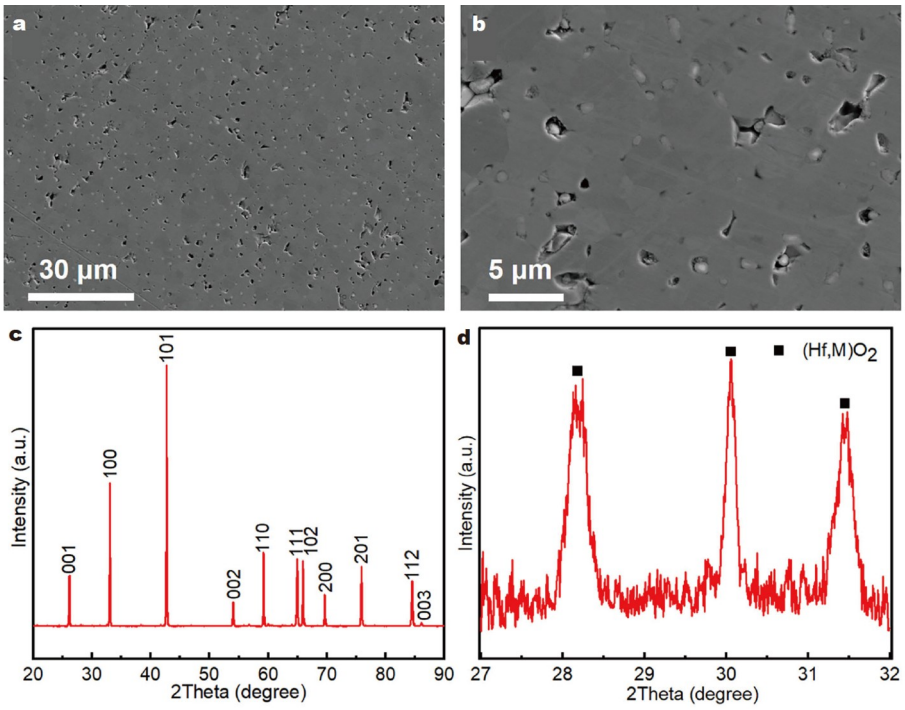


**Figure 1** SEM images of polished $(Ti_{0.2}Zr_{0.2}Nb_{0.2}Hf_{0.2}Ta_{0.2})B_2$ ceramics at different magnifications: (a) 1000×, (b) 4000×. (c) XRD patterns of HEB after SPS, showing the presence of diffraction peaks related to unreacted oxides (d).

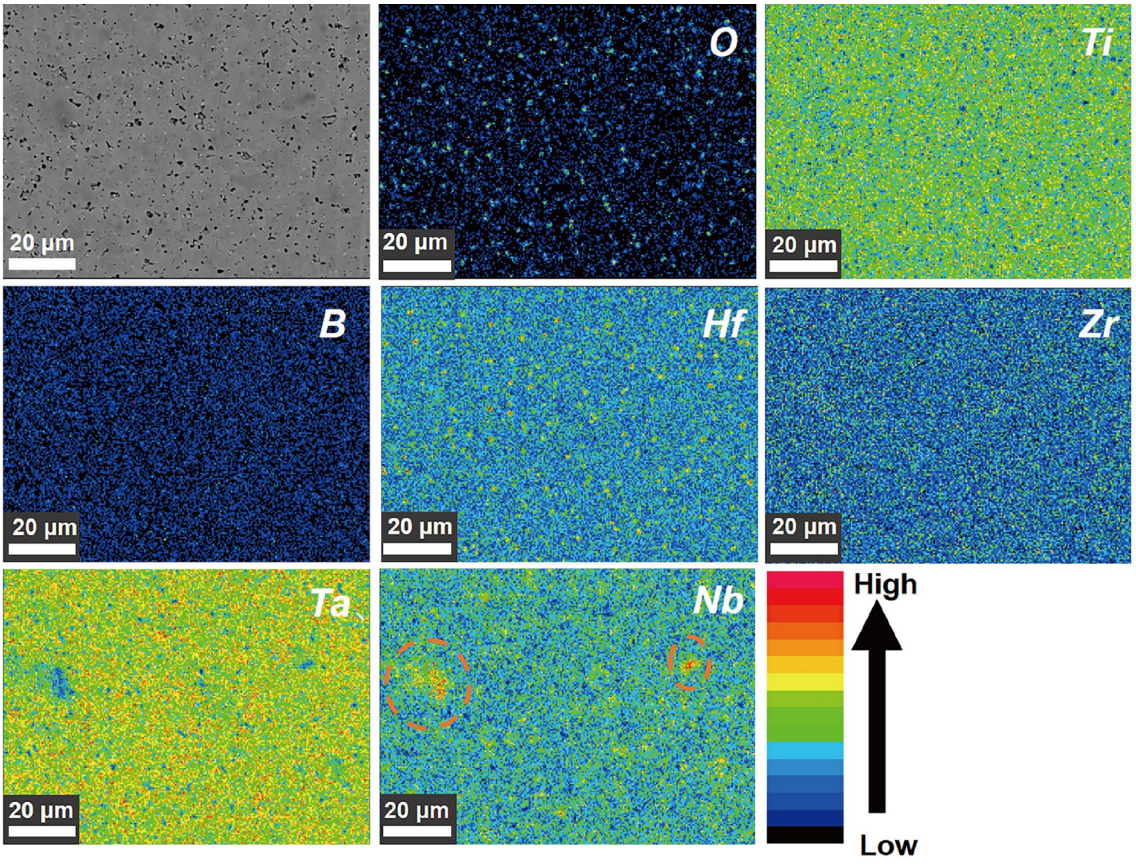


**Figure 2** WDS-mapping of HEB, revealing most of the metallic elements are evenly distributed, but some niobium elements are concentrated. The existence of oxides is also apparent.

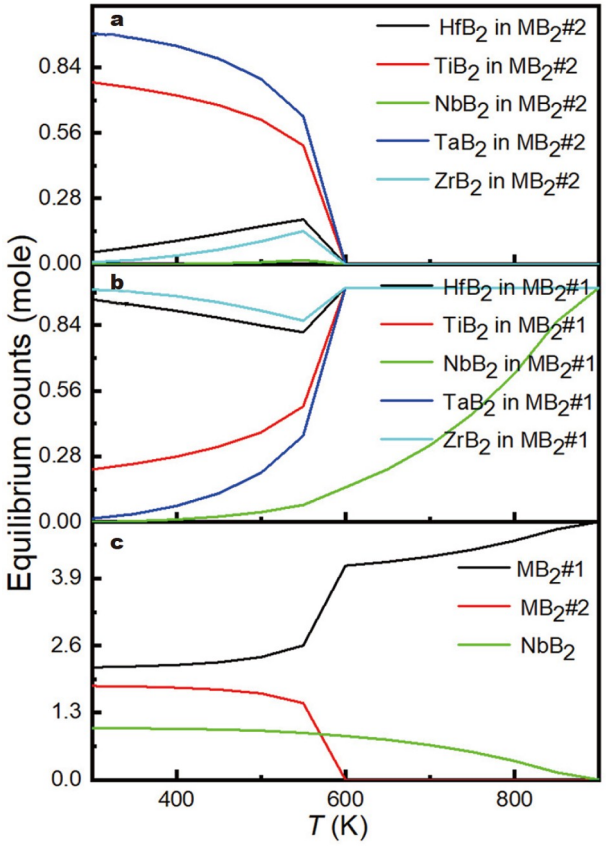


**Figure 3** (a) Equilibrium amounts of $MB_2$#1, $MB_2$#2 and $NbB_2$ as a function of temperature at 1 atm (1 atm = 101.3 kPa), starting from mixtures containing 1 mol $HfB_2$, 1 mol $NbB_2$, 1 mol $TaB_2$, 1 mol $TiB_2$ and 1 mol $ZrB_2$. The change of compositions in $MB_2$#1 (b), $MB_2$#2 (c) with temperature.

are a bit higher in $MB_2$#2. In addition to $MB_2$#1 and $MB_2$#2, the separated $NbB_2$ phase was also predicted to be favorable at lower temperatures, suggesting the dissolution of $NbB_2$ into HEBs is more difficult compared with the other diborides. At enough high temperatures, $MB_2$#1, $MB_2$#2, and $NbB_2$ could fully merge into a single HEB phase. The SPS temperature (2000°C) is much higher than the calculated temperature required for the formation of a single HEB phase; nevertheless, the Nb-rich region is still observed in the SPSed HEBs, revealing the fact that the incorporation of Nb into (Ti, Zr, Hf, Ta)$B_2$ is also restricted due to some kinetic factors.

Fine-scale microstructural analysis was carried out by scanning TEM (STEM), as shown in Fig. 4. According to the energy dispersive X-ray spectroscopy (EDS) mapping and the contrast of different phases suggested by high-angle annular dark field (HAADF) images (Fig. 4a), three distinct regions could be clearly recognized. In the HEB matrix, various metal elements are homogenously distributed without noticeable preferential aggregation. Similar to the WDS results, the spherical particles contain a significant amount of oxygen and hafnium. STEM-EDS mappings also suggest they are rich in zirconium; however, Ti, Ta and Nb atoms can only slightly dissolve into the oxide. The third phase (Area 3 arrowed in Fig. 4a) in a darker contrast located between the HEB matrix and the oxide was detected; nevertheless, it mainly contains light elements and its elemental composition is hard to be explored by EDS. For this reason, the EELS spectra from different areas were collected and compared (Fig. 4e). EELS analysis indicates that Area 3 contains boron and carbon with K edge of 188 and 284 eV, respectively. Therefore, it is more likely to be the unreacted $B_4C$. The coexistence of $B_4C$ and (Hf,Zr)$O_2$ suggests the carbo/boro-thermal process did not proceed to completion within 1 h at 1650°C. Recorded EELS pattern of boron carbide consists of pre-peaks at ~190 eV and convoluted peaks from 193 to 205 eV. From Area 3 labeled in Fig. 4e, a broadening of the convoluted peaks was seen, indicating the π-bonding in $B_4C$ has been significantly weakened during the process of powder synthesis and densification. Residual $B_4C$ grains lower the theoretical density value of HEB, which might explain the discrepancy on their porosity determined by the water replacement method and image analysis. Regarding the EELS pattern of spherical oxide particles (region 1 in Fig. 4a, e), in addition to the oxygen core loss (O-K edge, 531.75 eV), various signals could be recognized, e.g., B-K edge (188 eV), C-K edge (284 eV), Hf-$N_{4,5}$ edge (214 eV), Zr-$M_3$ edge (328 eV) and Zr-$M_2$ edge (340.25 eV). The EELS result suggests that, in addition to Ti, Ta, and Nb, certain amounts of boron and carbon atoms were also incorporated into the spherical oxides.

Fig. 4b represents the high-resolution TEM (HRTEM) image of the HEB matrix along the zone axis of $[0\bar{1}0]$, their interplanar spacings (0.2167 and 0.1471 nm) are consistent with the (101) and (102) planes of HEB, as suggested by the XRD pattern (Fig. 1c, 0.211 and 0.144 nm). Interplanar spacings of an oxide particle (0.2278 and 0.1653 nm) match the (210) and $(\bar{1}13)$ planes of $HfO_2$ in the XRD pattern (Fig. 1d, 0.227, and 0.165 nm) as well. Oxides and adjacent HEB grains are tightly bonded, and clean boundary between them is found according to HRTEM observations (Fig. 4d).

### Mechanical properties

Typical properties of as-sintered HEBs are listed in Table 1 and the RT mechanical properties of existing ($Ti_{0.2}Zr_{0.2}Nb_{0.2}Hf_{0.2}$-$Ta_{0.2}$)$B_2$ ceramics have been summarized (Table 2) [31–33]. Due to the remaining $B_4C$ and pores, the as-measured density (8.04 g $cm^{-3}$) for HEBs sintered in this study is comparable to or slightly lower than those (7.67–8.29 g $cm^{-3}$) reported in the literature [31,32], so do the elastic modulus values. As expected, the presence of pores and oxides reduces the hardness of HEB as well. Vickers hardness of HEBs indented under a load of 1.96 N reaches 18.7 GPa in this work, slightly lower than the denser counterparts, for example, 20.5 ± 1.0 GPa measured from ($Zr_{0.2}Ta_{0.2}Ti_{0.2}Nb_{0.2}Hf_{0.2}$)$B_2$ ceramics with a relative density (*r. d.*) of 99.1% and 22.4 ± 0.6 GPa with a *r. d.* of 97.9% [14,15,27], but it still has advantages compared with single-component diboride ceramics or less dense ($Zr_{0.2}Ta_{0.2}Ti_{0.2}Nb_{0.2}Hf_{0.2}$)$B_2$ ceramics with relative densities of 94% (16.4 ± 0.5 GPa) and 92.2% (17.5 ± 1.2 GPa) [26,34].

It is well known that the hardness tends to decrease as the indentation size increases at a larger scale, which is known as indentation size effects (ISE). Surprisingly, the hardness of HEBs in this study does not have an obvious tendency to decrease as the load increases (Fig. 5a), i.e., no typical ISE phenomena were observed. The averaged hardness values measured under loads of 1.96, 4.9, 9.8, 19.6, and 49 N are 18.7, 18.1, 17.3, and 17.7 GPa, respectively. The hardness value gradually stabilizes after the load reaches 4.9 N. Considering a hardness value should be determined by the asymptotic region of the hardness-load curve,

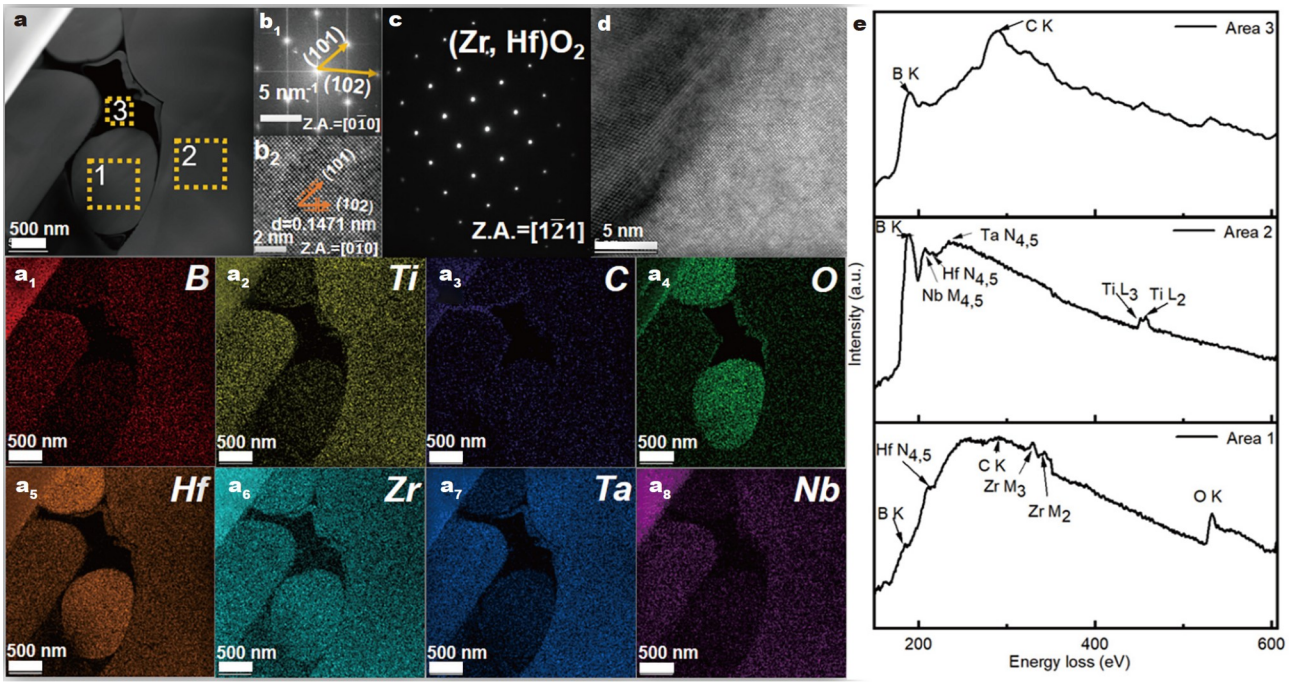


**Figure 4** (a) HAADF images of HEB showing the existence of oxides. HRTEM of one HEB grain ($b_2$) and fast Fourier transform (FFT) of $b_2$ ($b_1$). (c) Electron diffraction of an oxide grain and (d) a clean oxide/HEB grain boundary. (e) The EELS spectra of the corresponding areas squared 1, 2 and 3 in (a). STEM-EDS mappings of (a) are displayed in ($a_1$–$a_8$).

**Table 1** Properties of HEBs spark plasma sintered in this work

| Density (g cm$^{-3}$) | Relative density | $E$ modulus (GPa) | $G$ modulus (MPa) | Fracture toughness (MPa m$^{1/2}$) | | Flexural strength (MPa) | | |
|---|---|---|---|---|---|---|---|---|
| | | | | Load = 19.62 N | Load = 49.05 N | RT | 1600°C | 1800°C |
| 8.04 | 97.2% | 508.5 | 216.6 | 3.4 ± 0.1 | 4.2 ± 0.2 | 400.4 ± 47.0 | 695.9 ± 55.9 | 751.6 ± 23.2 |

**Table 2** Comparisons of mechanical properties and critical crack sizes for different HEBs

| Sample composition | Densification parameters | Strength (MPa) | Fracture toughness (MPa m$^{1/2}$) | Critical crack size (μm) | Grain size (μm) | Ref. |
|---|---|---|---|---|---|---|
| $(Ti_{0.2}Zr_{0.2}Hf_{0.2}Nb_{0.2}Ta_{0.2})B_2$ | SPS at 1800°C | 339 ± 17 | 3.8 ± 0.4 | 64.4 | 4.1 | [31] |
| $(Ti_{0.2}Zr_{0.2}Hf_{0.2}Nb_{0.2}Ta_{0.2})B_2$-SiC | – | 447 ± 45 | 4.9 ± 0.3 | 60.0 | 2.7 | [31] |
| $(Hf,Mo,Nb,Ta,W,Zr)B_2$ | 2000°C/50 MPa | 528 ± 53 | 3.9 ± 1.2 | 27.8 | 6.0 ± 2.0 | [32] |
| $(Hf_{0.25}Zr_{0.25}Ta_{0.25}Sc_{0.25})B_2$ | 2000°C/50 MPa | 454 ± 6 | 3.9 ± 0.4 | 23.5 | 2.2 ± 1.7 | [33] |
| $(Ti_{0.2}Zr_{0.2}Hf_{0.2}Nb_{0.2}Ta_{0.2})B_2$ | 2000°C/50 MPa | 400.4 ± 47.0 | 4.2 ± 0.2 | 36.6 | 3.0 ± 0.3 | This work |

4.9 N is suitable to be chosen as the ISE-boundary for the high-entropy diboride ceramics.

Based on the proportional specimen resistance (PSR) model developed by Li and Bradt [37], the true value of Vickers hardness (HV), load ($P$), and the indentation size ($d$) obeys Equation (1). For example, the actual hardness value measured under a load of 19.62 N is 17.3 ± 0.3 GPa, which is close to 17.4 GPa calculated from Equation (1).

$$HV_{true} = 7.99\frac{P}{d^2}. \quad (1)$$

The ISE effect originates from the increasing strain gradient in the smaller indentation. Larger strain gradients increase the hardness by increasing flow stress, which hinders the further expansion of indentation through dislocation blocking. In this study, it is worth noting that in contrast to a smooth quadrilateral concave surface obtained by forcing a pyramid diamond indenter, lots of cracks on the four triangular faces of the quadrangular pyramid can be found. In the indents obtained with loads of 0.2 and 0.5 kg, the cracks appear less and the distribution is irregular (Fig. 5c). In the indents obtained with loads of 1 and 2 kg, more cracks appear, gradually occupying the four triangular faces. Most interestingly, under a load of 5 kg, the cracks regularly occupy the four triangular faces of the indentation in a closed rhombus shape. The larger the indentation, the more cracks on the four triangular faces. Strain gradients around the indentation are hard to be determined, but their levels should be reduced when cracks are initiated in the indented zones. This point might explain why the ISE is not apparent in this material.

### High-temperature flexural strength

The RT flexural strength and fracture toughness for HEBs in this

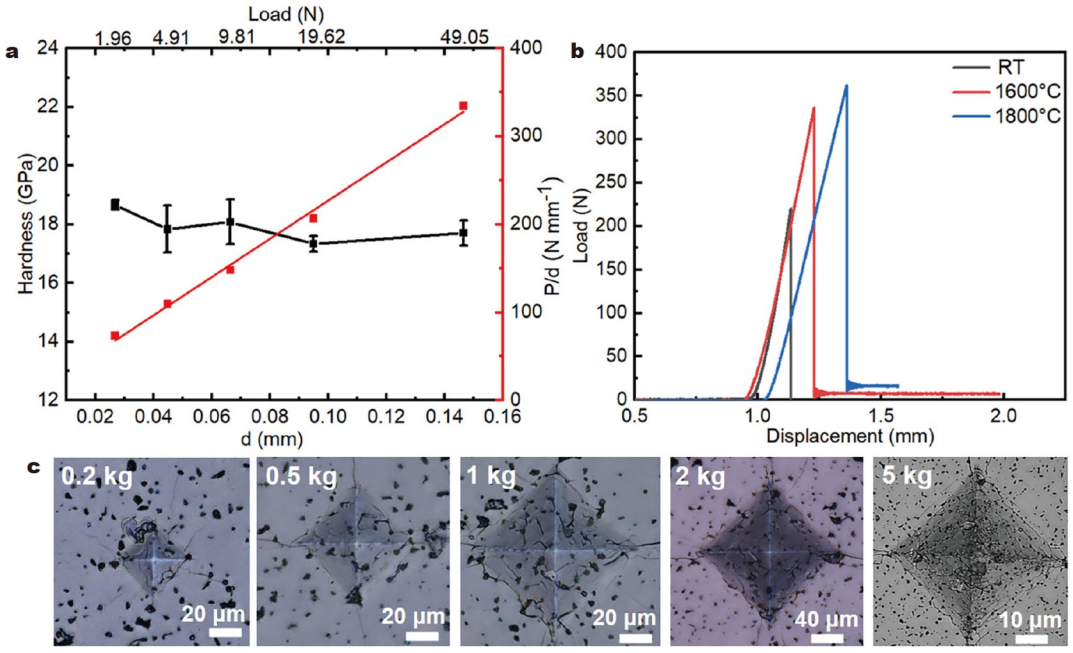


**Figure 5** (a) Vickers hardness of HEB under different loads and their applied testing loads *versus* indentation sizes. (b) Load-displacement curves for HEB at different temperatures. (c) Indentation morphologies for HEB under different loads from 0.2 to 5 kg using Keyence digital microscope, revealing the presence of cracks in the indentation zone.

study were determined to be 400.4 ± 47.0 MPa and 4.2 ± 0.2 MPa $m^{1/2}$—both values are slightly higher than the reported values in a range of 322–356 MPa and 3.8–3.9 MPa $m^{1/2}$ (Table 2). Unlike the studies in metals, the high-entropy effects do not lead to the strengthening of ceramics at RT, whereas reported values from monolithic $ZrB_2$ and $TiB_2$ ceramics [34] are even higher than those from HEBs [38,39]. To seek the reasons, the critical crack length was calculated according to Equation (2). The critical crack size of the HEB prepared in this work is 36.6 μm, relatively low among values reported in other HEB ceramics (27.8–64.4 μm). The results suggest the $\alpha_{cr}$ is much larger than the largest grain size in HEBs (~6.5 μm); therefore, the fracture of HEBs should be initiated from large defects existing in the ceramic body, possibly from machining generated cracks on the tensile surface of HEBs.

$$\alpha_{cr} = \frac{K_{IC}^2}{\pi\sigma_f^2}. \quad (2)$$

Interestingly, the flexural strength of HEBs becomes larger at higher temperatures. The three-point flexural strengths of HEBs at RT, 1600, and 1800°C are 400.4 ± 47.0, 695.9 ± 55.9, and 751.6 ± 23.2 MPa. All load/displacement plots displayed in Fig. 5b for HEBs were kept completely linear before the fracture point, regardless of the testing temperature. Comparing the curves (Fig. 5b), slope changes are very limited for samples tested at RT and 1800°C, implying that the decrease of stiffness or elastic modulus for HEBs is unremarkable in this temperature range. This point is quite different from $ZrB_2$ ceramics, in which the drop of modulus occurs at ~1300°C and the strength retention is ~60% at 1600°C [19,40–42].

The fracture surface morphology for HEBs was studied by SEM to determine the crack propagation mechanisms (Fig. 6). At RT, HEBs show typical transgranular fracture behavior, as most HEB/HEB grain boundaries are hard to be identified (Fig. 6$a_1$). From the enlarged images in Fig. 6$a_2$, $a_3$, spherical oxide grains were observed which were bonded to the HEB matrix *via* $B_4C$ showing a darker contrast, in agreement with the TEM results (Fig. 4d). With elevating testing temperatures to 1600 and 1800°C, more grains were fractured intergranularly (Fig. 6$b_1$–$b_3$, $c_1$–$c_3$). The competition between transgranular and intergranular strengths determines the type of fracture in ceramics. They both decrease with the increasing temperature. However, the latter usually decreases more rapidly. At RT, the greater intergranular strength leads to the predominance of transgranular fracture in HEBs, whilst intergranular fracture was observed when it was fractured at 1600 and 1800°C, suggesting the larger transgranular strength at higher temperatures.

The surface morphologies of HEBs fractured at different temperatures are compared in Fig. 7, and corresponding three-dimensional (3D) images were rendered into a color scale, which maps higher elevations in red and lower elevations in blue. As mentioned earlier, the calculated critical crack size of HEBs at RT (36.6 μm) is significantly larger than their grain size, suggesting the existence of flaws in test ceramic bodies. In fact, failure origins in semi-ellipsoidal shape were observed from the tensile surface of HEBs failed at RT (arrowed in Fig. 7$a_1$). As such preexisting defects were not found in HEBs failed at 1600 and 1800°C, the strength improvement (from 400.4 ± 47.0 MPa at RT to 751.6 ± 23.2 MPa at 1800°C) is probably related to the crack healing or residual stress relief on the bars during the test at higher temperatures, as observed in other structural ceramics [43–46].

According to Fig. 7, fracture surfaces of HEBs are rather rough, the distance between the highest and lowest points is ~0.6 mm at RT (Fig. 7a) and the values became even larger at 1600 and 1800°C (Fig. 7b, c), implying large energy was released during fracture. Furthermore, as arrowed in Fig. 7$a_1$, $c_1$, for HEB-RT and HEB-18, characteristic lips on the surface opposite

  

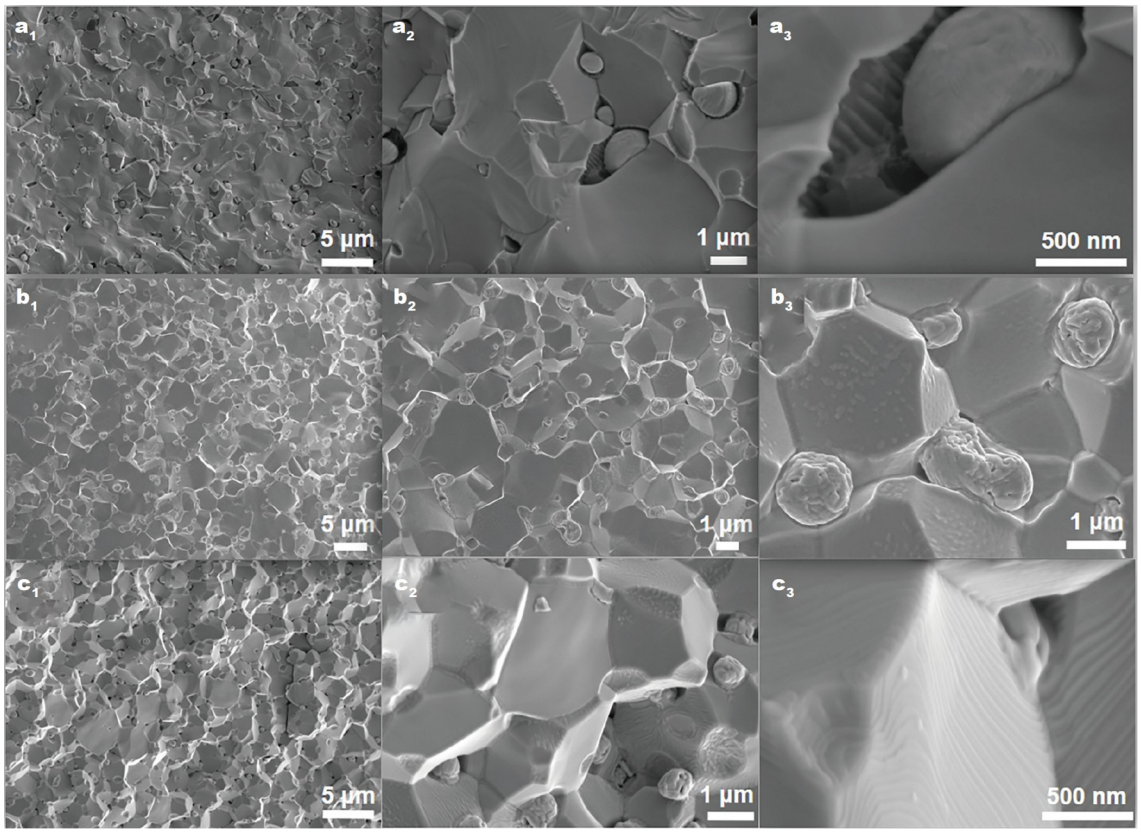


**Figure 6** Fracture surfaces of HEBs fractured at different temperatures with different magnifications: ($a_1$–$a_3$) RT; ($b_1$–$b_3$) 1600°C; ($c_1$–$c_3$) 1800°C.

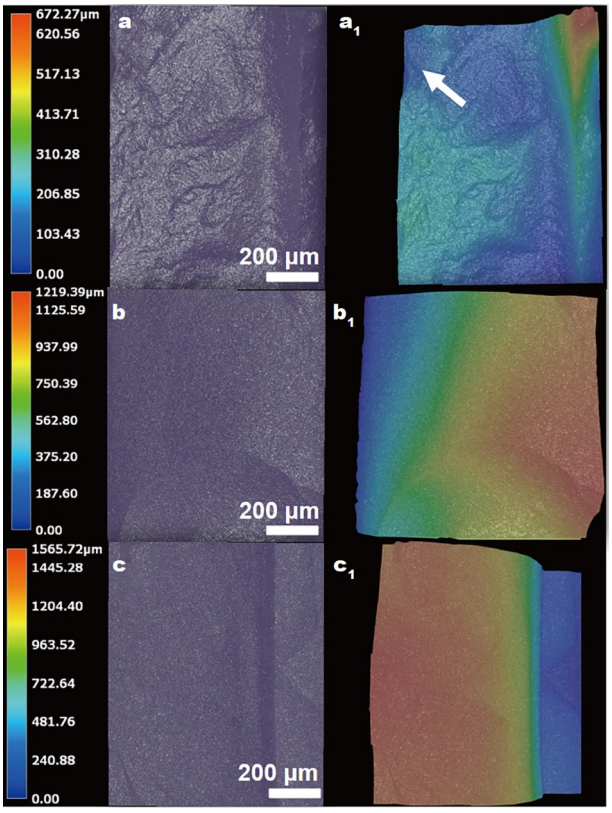


**Figure 7** Fracture surfaces and corresponding topography images of as-fabricated HEB failed at different temperatures: (a) RT; (b) 1600; (c) 1800°C. A crack origin was arrowed in $a_1$.

the original flaw were found, which are known as cantilever curls. During flexural tests, the stress status of the specimens varies across the sample: tensile stress should exist on their upper surface and the lower part is in compression. Therefore, when the speed for crack propagation is comparable to that of stress waves, the stress status from the crack front might change rapidly from compression to tension at the rear surface, causing the crack to wander out of its original plane (cantilever curls). Thermal fractures usually do not have compression curls because of the softening and grain sliding. The existence of cantilever curls further confirmed the excellent stiffness of HEBs even at 1800°C, contributing to their excellent strength as well.

**Mechanism of strength retention at 1800°C**

To further explore the strengthening mechanism of HEBs at higher temperatures, an area of 4 μm × 6 μm located at the tensile surface near the fractured part of HEB-18 was cut by FIB. TEM analysis results of this region are summarized in Fig. 8. HEB, oxide, and residual $B_4C$ grains were identified by electron diffractions (Fig. 8c–e), separately. According to the STEM-EDS mappings (Fig. 8$a_1$–$a_8$), different metallic elements are homogeneously distributed in the HEB matrix; however, the oxide grains are only rich in Hf, Zr and Ta. The latter point is different from the previous observation (Fig. 4$a_1$–$a_8$): the oxides are mainly composed of Hf, Zr and O in HEB-RT. Apparently, the diffusion of Ta atoms from HEB matrix to oxide grains took place during the flexural test hold at 1800°C.

Comparing Fig. 4a with Fig. 8a, it seems that the porosity in HEB-18 becomes higher than that in HEB-RT. TEM images with a higher magnification indicate that the residual $B_4C$ in HEB was

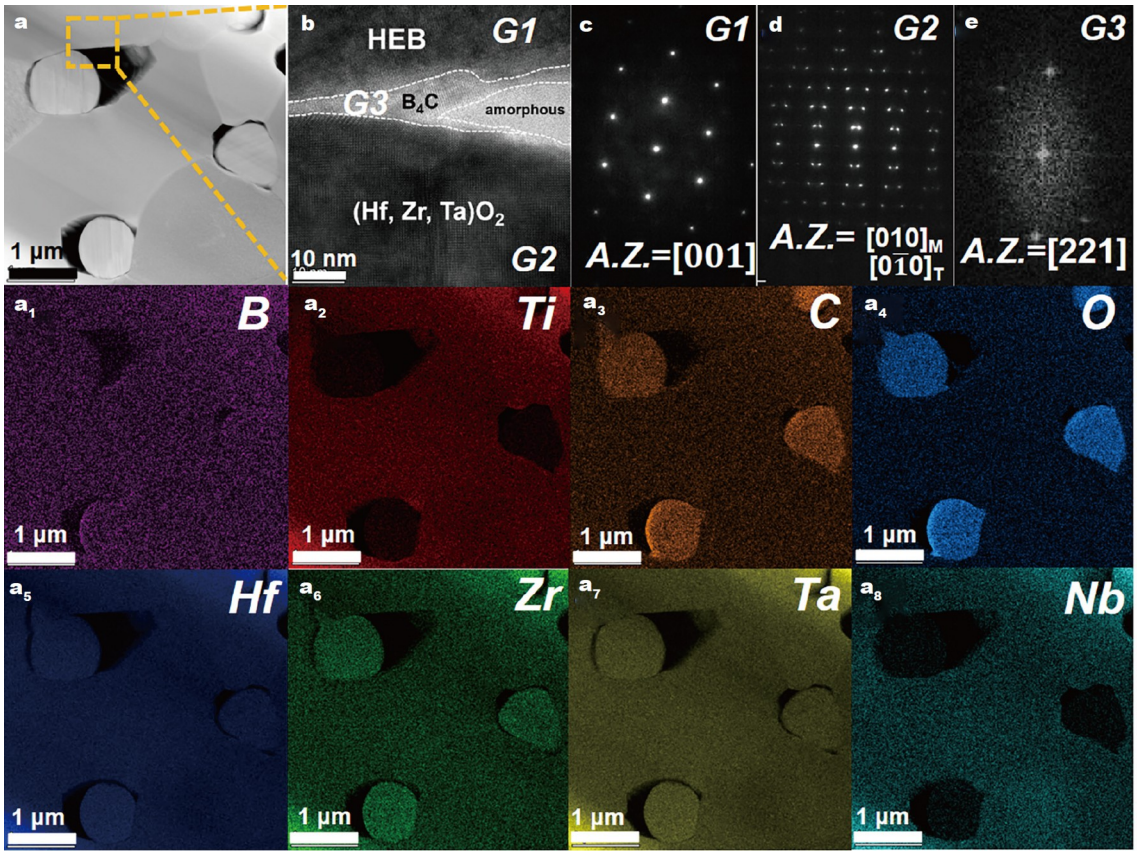


**Figure 8** (a) HAADF images of HEB fractured at 1800°C. The TEM slice was picked up from a region near the fracture and tensile surface by FIB. An enlarged region in (a) is shown in (b). Electron diffractions of grains (G1, G2 and G3) labelled in (b) are displayed in (c–e), which correspond to HEB, (Hf,Zr,Ta)$O_2$ and $B_4C$, respectively. STEM-EDS mappings of (a) are shown in ($a_1$–$a_8$).

partially oxidized during the bending test (Fig. 8b and Fig. S1), as a thin layer of amorphous phase appeared on top of the $B_4C$ grain and the size of $B_4C$-rich region became smaller as well. Zooming into regions with cracks and pore edges in HEB-18 (Fig. 9a–c), TEM observations only found very limited dislocation lines around them. Filtered FFT images (Fig. 9b, c, e) also suggested the low dislocation density in the HEB matrix, i.e., no trace of creep or plastic deformation occurred just adjacent to the crack front or pore edge. Resulting from the high entropy, i.e., lattice distortion and solid solution strengthening effects, HEB should exhibit a larger lattice resistance to dislocation movement, which also increases their yield strength. However, the lattice resistance (Peierls stress) decreases linearly with increasing temperature [47]; therefore, this effect itself could not explain the slightly higher strength values at HEB-18 compared with that of HEB-16.

As mentioned earlier, oxides were closely bonded with the HEB matrix in HEB-18; otherwise, the diffusion process of Ta into the oxides would be very extremely difficult. Moreover, Hf, Zr, Ta, boron, and carbon atoms were dissolved in the oxides, so the entropy and refractory nature of the oxides must be increased in HEB-18. It can be observed that as the temperature increases, the shape of the oxide particles has also been slightly changed (Fig. 6). Considering some oxides were isolated by $B_4C$ in HEB-RT, the better adhesion of HEB/oxides in HEB-18 might contribute to their better strength levels at 1800°C further, although other effects, in terms of residual stress recovering, crack healing, etc., might coexist and worth investigating in a future study. This work demonstrates that ($Ti_{0.2}Zr_{0.2}Nb_{0.2}Hf_{0.2}Ta_{0.2}$)$B_2$ high-entropy ceramics containing oxide particles as second phase own excellent high-temperature strength, which is inconsistent with conventional viewpoints that the presence of oxide impurities in diboride ceramics will deteriorate their high-temperature mechanical properties.

## CONCLUSION

In summary, nearly dense quinary high-entropy diboride ceramics were obtained by SPS, and their microstructure was carefully analyzed. RT mechanical properties were reported and high-temperature flexural strength up to 1800°C was investigated. Following conclusions could be drawn regarding this study:

(1) ($Ti_{0.2}Zr_{0.2}Nb_{0.2}Hf_{0.2}Ta_{0.2}$)$B_2$ ceramics (HEBs) with 2 vol% (Hf,Zr)$O_2$ and residual $B_4C$ (<1 vol%) could be densified at 2000°C/50 MPa for 10 min using high-entropy diboride powders synthesized from the BCTR approach.

(2) As-densified ($Ti_{0.2}Zr_{0.2}Nb_{0.2}Hf_{0.2}Ta_{0.2}$)$B_2$ ceramics exhibit a moderate elastic modulus of 503 GPa, fracture toughness of 4.2 ± 0.2 MPa $m^{1/2}$ and four-point flexural strength of 400.4 ± 47.0 MPa at RT. Due to the existence of porosity and oxide phase with lower hardness, HEBs show decreased hardness of 17.7 GPa at 5 kg. No representative ISEs were measured as cracks were seen in the indentation zone which might reduce the strain gradient.

(3) The four-point flexure strength of ($Ti_{0.2}Zr_{0.2}Nb_{0.2}Hf_{0.2}Ta_{0.2}$)$B_2$ ceramics increased with temperature, from 400.4 ±

  

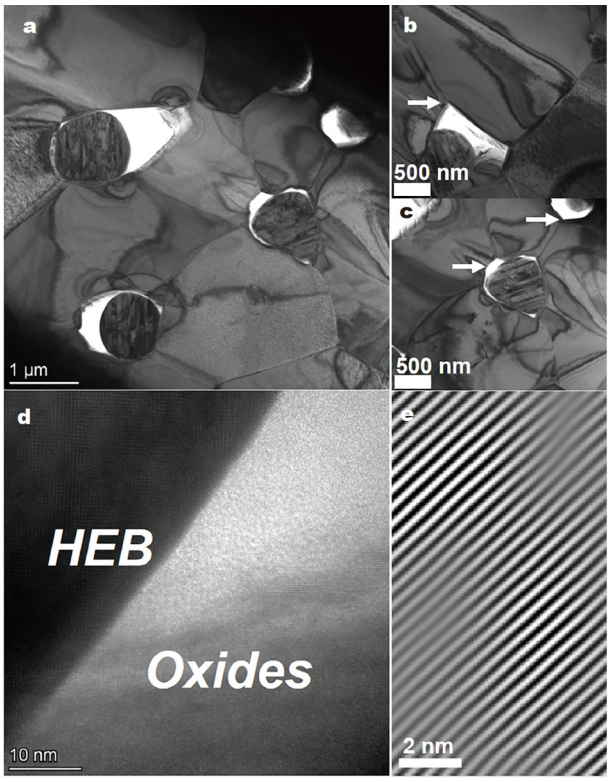


**Figure 9** (a) TEM images of HEB fractured at 1800°C showing plenty of pores and cracks. (b, c) Bright field images around pores and cracks with different magnifications. FFT of an HEB grain in (c) is shown in (d), indicating limited dislocations exist near the crack front.

47.0 MPa at RT to 751.6 ± 23.2 MPa at 1800°C. The high strength retention should be contributed by but not limited to (i) lattice distortion effect which retards the dislocation motion and avoids the possible plastic deformation around the crack tip; (ii) excellent stiffness of HEB at high temperatures; (iii) refractory nature of the oxides left in the HEB matrix, which tightens the HEB/oxides grain boundaries *via* diffusion of Ta atoms from HEB to the oxide during the test; (iv) strength recovery by healing the surface flaws at higher testing temperatures.

**Received 18 September 2022; accepted 14 October 2022; published online 10 January 2023**


1 Binner J, Porter M, Baker B, *et al.* Selection, processing, properties and applications of ultra-high temperature ceramic matrix composites, UHTCMCs—A review. Int Mater Rev, 2019, 65: 389–444
2 Fahrenholtz WG, Binner J, Zou J. Synthesis of ultra-refractory transition metal diboride compounds. J Mater Res, 2016, 31: 2757–2772
3 Paul A, Binner J, Vaidhyanathan B, *et al.* UHTC composites for hypersonic applications. Am Ceram Soc Bull, 2012, 91: 22–29
4 Fahrenholtz WG, Hilmas GE, Talmy IG, *et al.* Refractory diborides of zirconium and hafnium. J Am Ceramic Soc, 2007, 90: 1347–1364
5 Zhang X, Wang Z, Sun X, *et al.* Effect of graphite flake on the mechanical properties of hot pressed $ZrB_2$-SiC ceramics. Mater Lett, 2008, 62: 4360–4362
6 Wang Z, Wang S, Zhang X, *et al.* Effect of graphite flake on microstructure as well as mechanical properties and thermal shock resistance of $ZrB_2$-SiC matrix ultrahigh temperature ceramics. J Alloys Compd, 2009, 484: 390–394
7 Wang Z, Hong C, Zhang X, *et al.* Microstructure and thermal shock behavior of $ZrB_2$-SiC-graphite composite. Mater Chem Phys, 2009, 113: 338–341
8 Ma HB, Zou J, Lu P, *et al.* Oxygen contamination on the surface of $ZrB_2$ powders and its removal. Scripta Mater, 2017, 127: 160–164
9 Pellegrini C, Balat-Pichelin M, Rapaud O, *et al.* Oxidation resistance and emissivity of diboride-based composites containing tantalum disilicide in air plasma up to 2600 K for space applications. Ceramics Int, 2022, 48: 27878–27890
10 Harrington GJK, Hilmas GE, Fahrenholtz WG. Effect of carbon on the thermal and electrical transport properties of zirconium diboride. J Eur Ceramic Soc, 2015, 35: 887–896
11 Lonergan JM, Fahrenholtz WG, Hilmas GE. Zirconium diboride with high thermal conductivity. J Am Ceram Soc, 2014, 97: 1689–1691
12 Fu Q, Zhang P, Zhuang L, *et al.* Micro/nano multiscale reinforcing strategies toward extreme high-temperature applications: Take carbon/carbon composites and their coatings as the examples. J Mater Sci Tech, 2022, 96: 31–68
13 Ni D, Cheng Y, Zhang J, *et al.* Advances in ultra-high temperature ceramics, composites, and coatings. J Adv Ceram, 2022, 11: 1–56
14 Feng L, Fahrenholtz WG, Hilmas GE. Processing of dense high-entropy boride ceramics. J Eur Ceramic Soc, 2020, 40: 3815–3823
15 Qin M, Gild J, Wang H, *et al.* Dissolving and stabilizing soft $WB_2$ and $MoB_2$ phases into high-entropy borides *via* boron-metals reactive sintering to attain higher hardness. J Eur Ceramic Soc, 2020, 40: 4348–4353
16 Zhang Y, Jiang ZB, Sun SK, *et al.* Microstructure and mechanical properties of high-entropy borides derived from boro/carbothermal reduction. J Eur Ceramic Soc, 2019, 39: 3920–3924
17 Dai FZ, Wen B, Sun Y, *et al.* Grain boundary segregation induced strong UHTCs at elevated temperatures: A universal mechanism from conventional UHTCs to high entropy UHTCs. J Mater Sci Tech, 2022, 123: 26–33
18 Feng L, Fahrenholtz WG, Brenner DW. High-entropy ultra-high-temperature borides and carbides: A new class of materials for extreme environments. Annu Rev Mater Res, 2021, 51: 165–185
19 Silvestroni L, Kleebe HJ, Fahrenholtz WG, *et al.* Super-strong materials for temperatures exceeding 2000°C. Sci Rep, 2017, 7: 1–8
20 Zou J, Zhang GJ, Kan YM. Formation of tough interlocking microstructure in $ZrB_2$-SiC-based ultrahigh-temperature ceramics by pressureless sintering. J Mater Res, 2009, 24: 2428–2434
21 Demirskyi D, Borodianska H, Suzuki TS, *et al.* High-temperature flexural strength performance of ternary high-entropy carbide consolidated *via* spark plasma sintering of TaC, ZrC and NbC. Scripta Mater, 2019, 164: 12–16
22 Csanádi T, Vojtko M, Dankházi Z, *et al.* Small scale fracture and strength of high-entropy carbide grains during microcantilever bending experiments. J Eur Ceramic Soc, 2020, 40: 4774–4782
23 Han X, Girman V, Sedlak R, *et al.* Improved creep resistance of high entropy transition metal carbides. J Eur Ceramic Soc, 2020, 40: 2709–2715
24 Shen XQ, Liu JX, Li F, *et al.* Preparation and characterization of diboride-based high entropy $(Ti_{0.2}Zr_{0.2}Hf_{0.2}Nb_{0.2}Ta_{0.2})B_2$-SiC particulate composites. Ceramics Int, 2019, 45: 24508–24514
25 Qin Y, Liu JX, Liang Y, *et al.* Equiatomic 9-cation high-entropy carbide ceramics of the IVB, VB, and VIB groups and thermodynamic analysis of the sintering process. J Adv Ceram, 2022, 11: 1082–1092
26 Gild J, Zhang Y, Harrington T, *et al.* High-entropy metal diborides: A new class of high-entropy materials and a new type of ultrahigh temperature ceramics. Sci Rep, 2016, 6: 37946
27 Zhang Y, Sun SK, Guo WM, *et al.* Fabrication of textured $(Hf_{0.2}Zr_{0.2}Ta_{0.2}Cr_{0.2}Ti_{0.2})B_2$ high-entropy ceramics. J Eur Ceramic Soc, 2021, 41: 1015–1019
28 Zhang Y, Guo WM, Jiang ZB, *et al.* Dense high-entropy boride ceramics with ultra-high hardness. Scripta Mater, 2019, 164: 135–139
29 Zhang SC, Hilmas GE, Fahrenholtz WG. Pressureless densification of zirconium diboride with boron carbide additions. J Am Ceramic Soc, 2006, 89: 1544–1550
30 Zou J, Zhang G, Kan Y, *et al.* Pressureless densification of $ZrB_2$-SiC composites with vanadium carbide. Scripta Mater, 2008, 59: 309–312
31 Liu JX, Shen XQ, Wu Y, *et al.* Mechanical properties of hot-pressed high-entropy diboride-based ceramics. J Adv Ceram, 2020, 9: 503–510


  

32 Murchie AC, Watts JL, Fahrenholtz WG, *et al.* Room-temperature mechanical properties of a high-entropy diboride. Int J Appl Ceramic Tech, 2022, 19: 2293–2299
33 Zhang Z, Zhu S, Liu Y, *et al.* Phase structure, mechanical properties and thermal properties of high-entropy diboride $(Hf_{0.25}Zr_{0.25}Ta_{0.25}Sc_{0.25})B_2$. J Eur Ceramic Soc, 2022, 42: 5303–5313
34 Gu J, Zou J, Sun SK, *et al.* Dense and pure high-entropy metal diboride ceramics sintered from self-synthesized powders *via* boro/carbothermal reduction approach. Sci China Mater, 2019, 62: 1898–1909
35 Spencer PJ. Development of a thermodynamic database for refractory boride, carbide, nitride and silicide systems. In: Materials Science & Technology 2017 Conference & Exhibition. Pittsburgh, 2017: 1230–1238
36 Saxena S, Spencer P, Drozd V. An alternative, environmentally friendly production process for refractory metal carbides and syngas using methane reduction of the oxide ores. Monatsh Chem, 2018, 149: 411–422
37 Li H, Bradt RC. The microhardness indentation load/size effect in rutile and cassiterite single crystals. J Mater Sci, 1993, 28: 917–926
38 Liu L, Hou Z, Zhao Y, *et al.* Fabrication of $ZrB_2$ ceramics by reactive hot pressing of ZrB and B. J Am Ceram Soc, 2018, 101: 5294–5298
39 Li LH, Kim HE, Son Kang E. Sintering and mechanical properties of titanium diboride with aluminum nitride as a sintering aid. J Eur Ceramic Soc, 2002, 22: 973–977
40 Zou J, Zhang GJ, Hu CF, *et al.* Strong $ZrB_2$-SiC-WC ceramics at 1600°C. J Am Ceram Soc. 2012, 95: 874–878
41 Zou J, Zhang GJ, Hu CF, *et al.* High-temperature bending strength, internal friction and stiffness of $ZrB_2$-20 vol% SiC ceramics. J Eur Ceramic Soc, 2012, 32: 2519–2527
42 Zou J, Zhang GJ, Vleugels J, *et al.* High temperature strength of hot pressed $ZrB_2$-20 vol% SiC ceramics based on $ZrB_2$ starting powders prepared by different carbo/boro-thermal reduction routes. J Eur Ceramic Soc, 2013, 33: 1609–1614
43 Ando K, Houjyou K, Chu MC, *et al.* Crack-healing behavior of $Si_3N_4$/SiC ceramics under stress and fatigue strength at the temperature of healing (1000°C). J Eur Ceramic Soc, 2002, 22: 1339–1346
44 Lange FF, Gupta TK. Crack healing by heat treatment. J Am Ceramic Soc, 1970, 53: 54–55
45 Lange FF, Radford KC. Healing of surface cracks in polycrystalline $Al_2O_3$. J Am Ceramic Soc, 1970, 53: 420–421
46 Luo W, Yan S, Zhou J. Ceramic-based dielectric metamaterials. Interdisciplinary Mater, 2022, 1: 11–27
47 Nabarro FRN. Fifty-year study of the Peierls-Nabarro stress. Mater Sci Eng-A, 1997, 234-236: 67–76


**Acknowledgements** This work was supported by the National Natural Science Foundation of China (52022072, 51972243, 92060202 and 52202067), the National Key R&D Programs (2021YFB3701400), Hubei Provincial Natural Science Foundation of China (Distinguished Young Scholars 2022CFA042), Independent Innovation Projects of Hubei Longzhong Laboratory (2022ZZ-10), and the Research Fund for Central Universities (2020IVB074 and 2021IVA094). The authors appreciate Dr. Junfeng Gu and Dr. Haiyue Xu for their help with sample preparations.

**Author contributions** All authors participated in the discussion of the results. Zou J conceived the idea of this work. Liu J, Yang QQ and Zou J performed the main experiments. Fu ZY and Wang WM provided resources and helped construct the framework of the manuscript. Yang QQ and Wang XG measured the high-temperature strength. Liu J and Zou J wrote the paper, which was revised by Wang WM and Fu ZY.

**Conflict of interest** The authors declare that they have no conflict of interest.

**Supplementary information** Supporting data are available in the online version of the paper.

**Jie Liu** is currently a Master's student at the State Key Laboratory of Advanced Technology for Materials Synthesis and Processing, Wuhan University of Technology. Her research focuses on the strengthening mechanisms and properties of high-entropy diboride ceramics.

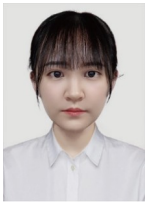

**Qing-Qing Yang** is currently a research assistant at the State Key Laboratory of Advanced Technology for Materials Synthesis and Processing, Wuhan University of Technology. Her research focuses on the microstructure control and ultra-high temperature mechanical properties of high-entropy ceramics.

**Ji Zou** is a professor at Wuhan University of Technology. He received his PhD degree from Shanghai Institute of Ceramics, Chinese Academy of Sciences. He has been active in the processing-structure-property correlation of ceramics and composites, especially for borides.

**Xin-Gang Wang** is a senior engineer at Shanghai institute of Ceramics, Chinese Academic of Sciences. He graduated from the same institute and worked from there since then. His current research interests include ceramics for extreme environments and the mechanical performances for coatings and fibers.

**Zheng-Yi Fu** is a chief professor and an academician of Chinese Academy of Engineering at the State Key Laboratory of Advanced Technology for Materials Synthesis and Processing, Wuhan University of Technology. He received his PhD degree from Wuhan University of Technology in 1994. His current research interests include advanced ceramics, composites and their bioprocess-inspired fabrication.

## 1800°C下具有优异高强度且含氧化物杂质的高熵二硼化物陶瓷

柳洁[1,2], 杨青青[1,3], 邹冀[1,2*], 王为民[1,2], 王新刚[3*], 傅正义[1,2*]

**摘要** 以硼热/碳热还原合成高熵二硼化物粉体为原料，在2000°C/单轴加压50 MPa条件下，经10分钟放电等离子烧结，成功制备了含有~2 vol%的氧化物和~1 vol%气孔的高熵$(Ti_{0.2}Zr_{0.2}Nb_{0.2}Hf_{0.2}Ta_{0.2})B_2$陶瓷(HEBs). 经研究确认，其中残留氧化物是固溶少量硼和碳的m-$(Hf,Zr)O_2$. 室温下HEBs的弹性模量、维氏硬度和断裂韧性分别为508.5 GPa、17.7 ± 0.4 GPa和4.2 ± 0.2 MPa $m^{1/2}$. 烧结得到的HEBs具有优良的抗弯强度，特别是其高温强度. HEBs在室温、1600和1800°C下的四点抗折强度分别为400.4 ± 47.0 MPa、695.9 ± 55.9 MPa和751.6 ± 23.2 MPa. 对1800°C下断裂的HEBs样品进行了失效分析，在其拉伸和断裂面附近区域，仅在裂纹尖端和孔隙边缘发现了数量有限的位错线的存在，没有观察到位错运动的痕迹. 本研究首次报道了高熵二硼化物陶瓷的高温强度，发现其强度直至1800°C并无衰减，并对其高温下的强韧化机制进行了有益的探讨.

  